CrossMark

ORIGINAL PAPER

Electrochemical response of several cathode configurations prepared with $Ba_{0.5}Sr_{0.5}Co_{0.8}Fe_{0.2}O_{3-\delta}$ and $Ce_{0.9}Gd_{0.1}O_{1.95}$ for IT-SOFC

Cristian Setevich[1,2] · Fernando Prado[1] · Alberto Caneiro[2]

Abstract The electrochemical response of $Ba_{0.5}Sr_{0.5}Co_{0.8}Fe_{0.2}O_{3-\delta}$ (BSCF) electrodes prepared by an acetic acid-based gel route has been investigated by impedance spectroscopy (IS) as a function of temperature ($400 \leq T \leq 900\ °C$) and oxygen partial pressure ($1 \times 10^{-3} \leq pO_2 \leq 1\ atm$). Several electrode configurations were studied using $Ce_{0.9}Gd_{0.1}O_{1.95}$ (GDC) as the electrolyte. These consisted of one BSCF layer (cell A), a BSCF layer with an intermediate porous GDC layer (cell B), and graded electrodes using a composite BSCF+GDC, with variations in the surface area of GDC (cells C and D). The optimum heat treatment for the electrode assemblages was determined to be around 850–900 °C. Analysis of the impedance spectra shows that at $T \geq 600\ °C$ a low frequency (LF) contribution, associated to the gas phase diffusion is systematically the rate-limiting step. All the electrodes show an intermediate frequency (IF) arc related to mixed processes. For cells A and B, the IF response is related to the oxide ion transfer at the electrode/electrolyte surface and the charge transfer at the electrode surface, while for cells C and D the mixed process involves the charge transfer and the molecular oxygen dissociation at the electrode surface.

✉ Fernando Prado
fernando.prado@uns.edu.ar

[1] Departamento de Física, Universidad Nacional del Sur and Instituto de Física del Sur, CONICET, Av. L. N. Alem, 1253, 8000 Bahía Blanca, Argentina

[2] Centro Atómico Bariloche, Comisión Nacional de Energía Atómica, Av. Bustillo, 9500, 8400 S. C. de Bariloche, Argentina

Introduction

Transition metal oxides with the perovskite crystal structure have been extensively studied in order to develop oxygen separation membranes and the cathode for intermediate temperature solid oxide fuel cells (IT-SOFC) [1, 2]. In particular, $Ba_{0.5}Sr_{0.5}Co_{0.8}Fe_{0.2}O_{3-\delta}$ (BSCF) was initially developed to be used as an oxygen separation membrane [3]. The replacement of half the Sr^{2+} by the larger alkaline earth Ba^{2+} in the A-site of the perovskite $SrCo_{0.8}Fe_{0.2}O_{3-\delta}$ leads to both an increase in the oxygen permeation flux across dense ceramic membranes, a quantity related to the oxide ion conductivity of the material [4] and to the stabilization of the cubic perovskite by preventing the crystal structure transformation from the cubic perovskite to the orthorhombic brownmillerite [5–7]. Furthermore, Shao and Haile [8] have reported an excellent performance of BSCF as cathode material for IT-SOFC. However, the pioneer work of Shao et al. [3] and later studies [9, 10] have pointed out the lack of long-term stability of the cubic BSCF at intermediate temperatures ($T < 850\ °C$) in air. The cubic phase results unstable and gradually transforms into a mixture of a cubic perovskite and a hexagonal phase [9, 10]. Also, the expansion coefficients of cobaltites [11] and BSCF [12] are larger than those of the electrolytes [12], causing the degradation of the electrode-electrolyte interface by thermal cycling and therefore reducing the performance of the cell [13, 14]. In spite of these issues, the polarization resistance [8, 15] and the power density values [8, 16–18] obtained for BSCF at intermediate temperatures are among the lowest and the highest, respectively, reported in the literature.

To reduce the expansion coefficient mismatch, a couple of strategies may be applied. One of these is the use of a composite [16, 19], a mixture of the oxide-mixed conductor and an electrolyte, or a graded electrode, where the composition of the cathode varies by steps from pure electrolyte to the oxide-

Springer

mixed conductor material [15, 20, 21]. Experimental data indicate that while the use of a composite material as electrode generally improves the polarization resistance [22–24], it reduces the electrical conductivity of the cathode [16, 21]. In any case, the optimum electrolyte/mixed conductor ratio for these configurations is affected by several factors such as the microstructure, preparation method, and chemical reaction between the materials forming the composite [25]. For the particular case of the composite BSCF+$Sm_{0.2}Ce_{0.8}O_{1.9}$ (SDC), the area specific polarization resistance at $T = 600$ °C was reported to be lower (0.064 Ω cm^2) than that of BSCF (0.099 Ω cm^2) in spite of the formation of a secondary phase at the electrode/electrolyte interface when the cells were prepared at $T \geq 1000$ °C [16].

Due to the relevance of BSCF as cathode material and the alternative of using the composite BSCF+GDC in order to improve the electrochemical performance of the cathode, we have evaluated and compared the electrochemical response to the oxygen reduction reaction of various electrode configurations, all prepared with BSCF, which was synthesized by an acetic acid-based gel route. By means of impedance spectroscopy, we determined the optimum heat treatment temperature for the preparation of the electrodes. The contributions to the polarization resistance due to the oxygen reduction reaction at the electrode as a function of T, pO_2, and the electrode design are also discussed.

Experimental

The BSCF material was prepared by an acetic acid-based gel route [26]. Stoichiometric amounts of $SrCO_3$, $BaCO_3$, $Co(CH_3COO)_2.4H_2O$, and $Fe(NO_3)_3.9H_2O$ were weighed and dissolved in acetic acid. Together with water and small amounts of hydrogen peroxide, the mixture was refluxed at $T \sim 80$ °C until a clear solution was obtained. The solvents were then evaporated until a dark gel was formed, which was first dried and later decomposed at 400 °C for 2 h. The resulting powder was fired at 750 °C for 24 h in air. We denominated this material BSCF-750. The cubic phase formation was monitored as a function of temperature performing an additional heat treatment at 800, 900, 1000, and 1100 °C during 8 h in air. After each heat treatment, the sample was cooled to 20 °C at a rate of 5 °C/min. The $Ce_{0.9}Gd_{0.1}O_{1.95}$ (GDC) material was synthesized by the combustion method. Stoichiometric amounts of Gd_2O_3 y $Ce(NO_3)_3.6H_2O$ were dissolved in acetic acid, the mixture was refluxed at $T \sim 80$ °C until a clear solution was obtained. Subsequently, the temperature was raised to approximately 300 °C, at which the ignition of the solution started.

X-ray diffraction (XRD) data were collected at room temperature with a Philips PW1700 diffractometer using Cu Kα radiation and a graphite monochromator from $2\theta = 10°$ to $80°$

with a counting time of 1 s per 0.02°. For crystal structure analysis of the BSCF sample heat treated at 1100 °C, XRD data were collected at room temperature with a counting time of 10 s per 0.02° and analyzed by the Rietveld method using the FullProf Program [27].

Linear expansion data were obtained on cylindrical samples of approximately 5.0 mm diameter and 7 to 10 mm height, from room temperature to 900 °C, using a LINSEIS L75PT Series dilatometer. Measurements consisted of a heating/cooling cycle between room temperature and 900 °C at 1 °C/min. Experimental data were corrected using Al_2O_3 as standard.

The polarization resistance of the BSCF electrodes was studied by impedance spectroscopy measurements on electrochemical cells using GDC as electrolyte and a symmetrical configuration in air. Commercial $Ce_{0.9}Gd_{0.1}O_{1.95}$ powder from Fuel Cell Materials was pressed into 12.5-mm-diameter disks, applying uniaxial pressure of 200 kg/cm^2, and sintered at 1350 °C during 4 h in air. After sintering, the electrolyte disks were approximately 9.8 mm in diameter and around 0.3 mm thick. The inks for electrode deposition were prepared by mixing the corresponding ceramic powders with ethanol, α-terpineol, polyvinyl butyral, and polyvinyl pyrrolidone in appropriate portions. Four electrode configurations were tested:

Cell A: The electrodes consisted of a single layer of the BSCF material heat treated at 750 °C sprayed onto dense GDC electrolyte.

Cell B: The electrodes consisted of two layers, the first made of porous GDC from Fuel Cell Materials (surface area 35.6 m^2/g) sprayed on the dense electrolyte and then heat treated at 1300 °C during 1 h. A second layer made of the BSCF material heat treated at 750 °C was sprayed onto the first layer.

Cell C: In this case the electrodes consist of an arrange of three layers, one of porous GDC similar to the one described in cell B, one of composite material prepared with BSCF+ GDC in a 1:1 weight ratio sprayed onto the porous GDC layer, and finally a BSCF layer sprayed onto the composite layer.

Cell D: The electrode configuration is similar to cell C. However, in this case, the porous GDC and the composite layers were prepared with GDC obtained from the combustion synthesis method (surface area 69.0 m^2/g).

Figure 1 shows the schematic of the four electrode configurations used for testing the polarization resistance. After the electrodes were deposited on the electrolyte, the symmetrical cells were heat treated at 750 °C during 1 h, in air, and subsequently cooled to 600 °C at a rate of 1 °C/min to determine the polarization resistance. The optimum heat treatment temperature for the electrode preparation was obtained by repeating this procedure between 750 and 950 °C by steps of 50 °C and finding the minimum polarization resistance value. Then, impedance spectroscopy measurements were performed varying

Fig. 1 Schematic of the electrode configurations used for impedance spectroscopy measurements. Porous GDC and composite layers in Cell D were prepared with GDC obtained by the combustion method
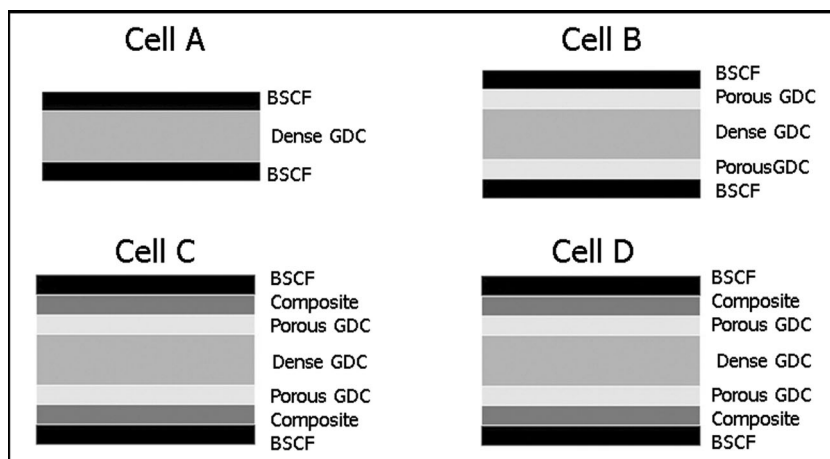
the temperature in the range of $400 \leq T \leq 950$ °C by steps of 50 °C and the oxygen partial pressure (pO$_2$) in the range $10^{-3} \leq pO_2 \leq 1$ atm by mixing Ar and O$_2$. The data acquisition was performed by an Autolab system PGSTAT-30 coupled to a module FRA2 in a frequency range of 1 MHz and 10^{-3} Hz. An ac signal of 10 mV was applied to the cell, under zero DC polarization. Platinum grids, slightly pressed on the porous electrodes using an Al$_2$O$_3$ tube, were used as current collectors. Impedance diagrams were analyzed using Z-view2 software [28].

The microstructure and thickness of the porous layers and interfaces were characterized by scanning electron microscopy (SEM) using a Phillips microscope 515.

Results and discussion

Phase formation, chemical compatibility, and expansion coefficient determination

Figure 2 shows the XRD patterns of the BSCF material prepared at 750 °C and subsequently heat treated at various temperatures (800, 900, 1000, and 1100 °C) during 8 h, in air. At 750 °C the chemical reaction is not yet complete and the BSCF-750 sample consists of a mixture of three phases: the 2H-hexagonal phase BaCoO$_3$ [29], a cubic phase of general composition Sr$_x$Ba$_{1-x}$Co$_{1-y}$Fe$_y$O$_{3-\delta}$, and an unknown phase with hexagonal symmetry [9, 10]. As the temperature increases, the fraction of the 2H-hexagonal phase decreases, finally vanishing at 900 °C, while the unknown phase is eliminated at 1000 °C. At $T \geq 1000$ °C, the sample becomes single phase, forming the cubic perovskite BSCF. Figure 2 shows the Rietveld refinement of the XRD data for the sample heat treated at 1100 °C using the cubic space group Pm-3m. The obtained lattice parameter was $a = 3.987$ (1) Å.

Reactivity tests were carried out on samples of BSCF-750 mixed with GDC in a 1:1 weight ratio and heat treated in the
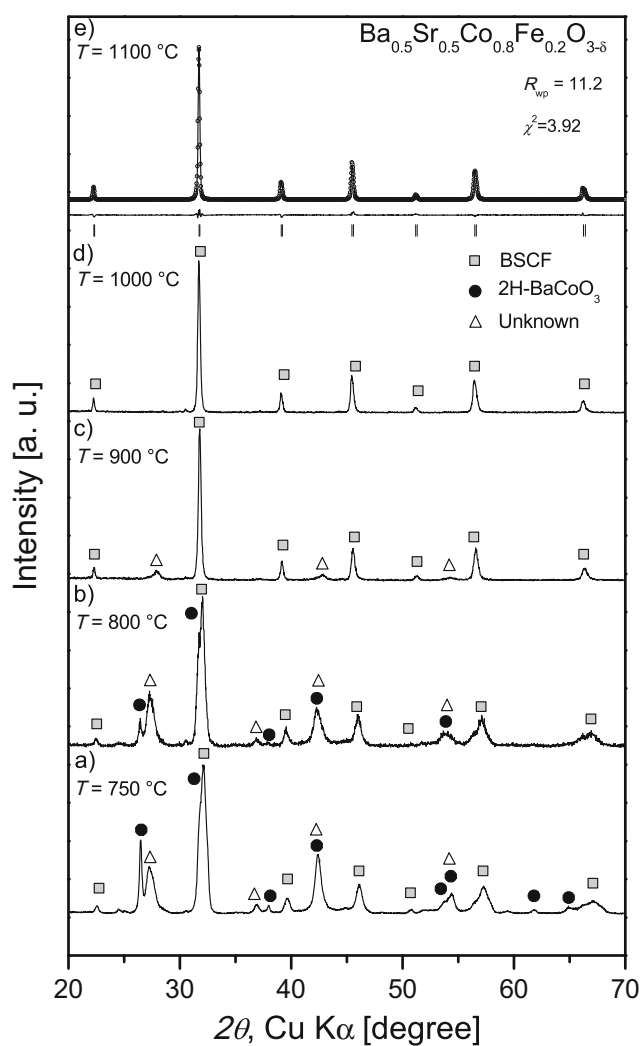

Fig. 2 BSCF cubic phase formation as a function of the heat treatment temperature monitored by XRD measurements. **a** Starting material heat treated at 750 °C during 24 h, in air, **b–e** The starting material heat treated at 800, 900, 1000, and 1100 °C, respectively, during 8 h. For the sample heat treated at 1100 °C (**e**), the experimental data (○), calculated profile (-), peak position (|), and the difference between observed and calculated profiles obtained from Rietveld analysis are included

temperature range $800 \leq T \leq 1000$ °C during 8 h in air. The XRD patterns of these samples are shown in Fig. 3. After the heat treatment at 800 °C, no evidence of chemical reactivity was detected (Fig. 3a, b). At $T \geq 900$ °C, minor reflections corresponding to the formation of the perovskite $BaCeO_3$ are clearly revealed at $2\theta \sim 41.2$° and 51°, along with the formation of the cubic BSCF perovskite. The intensities of $BaCeO_3$ reflections increase with temperature and, at the same time, BSCF reflections shift to higher angles indicating a decrease in its Ba content [16, 30]. The absence of reflections of Co/Fe oxides suggests that the BSCF phase could be slightly deficient in the A site [31].

The use of the composite BSCF+GDC between the electrolyte and BSCF helps to reduce the volume expansion, particularly the chemical expansion contribution [32] at temperatures above 400 °C, relieving adherence issues between the electrode and the electrolyte. This effect is shown in Fig. 4, where $\Delta L/L_0$ vs. T curves for pure GDC, the composite BSCF+GDC, and BSCF in the temperature range of $30 \leq T \leq 900$ °C, in air, are displayed. Clearly, as the content
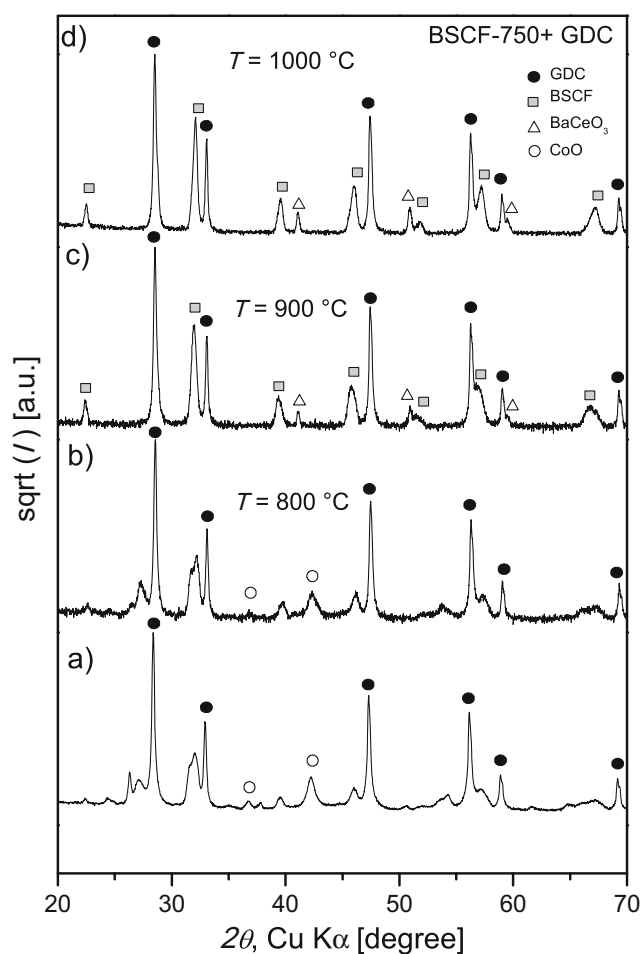
of GDC increases, the chemical expansion contribution of BSCF is progressively reduced. In Table 1, we have listed the linear expansion coefficient values for the temperature range $80 \leq T \leq 300$ °C, where the thermal expansion contribution predominates, and $400 \leq T \leq 900$ °C, where both the thermal and chemical expansion contributions are relevant. Finally, the total linear expansion was determined for $80 \leq T \leq 900$ °C, obtaining 18.6 (2), 15.0 (1), and 12.0 (1) × 10^{-6} K^{-1} for BSCF, the composite BSCF+GDC and GDC, respectively, in agreement with previous reports [19].

Optimization of the heat treatment temperature for the cathode preparation

The optimum heat treatment temperature for the assemblage of layers with BSCF-750 was monitored by impedance spectroscopy. Figure 5 shows the complex impedance spectra obtained at 600 °C for the four different cell configurations after the electrodes were heat treated at various temperatures between 750 and 950 °C. In this figure, the impedance spectra were shifted so that the low-frequency data intercept the x-axis at approximately $Z' = 0$. Systematically, the impedance spectra at 600 °C consist of two arcs, a low-frequency arc-denominated LF and a second arc in which we assigned to the intermediate frequency range and denominated IF. The LF arc barely changes with the heat treatment temperature; the same happens with the apex frequency, which remain at around 2 Hz. On the other hand, the polarization resistance due to the IF process at 600 °C strongly decreases as the electrode preparation temperature increases reaching the minimum value after the heat treatments at 850–900 °C, which is in agreement with the formation of the majority phase BSCF in the electrode (see Fig. 2). The Rp values obtained for cells A, B, C, and D at 600 °C were in the range $0.039 \leq R$p ≤ 0.05 Ω cm^2, which is unexpectedly narrow considering the variations in

Fig. 3 XRD patterns of BSCF-750 mixed with GDC from Fuel Cell Materials and heat treated during 8 h, in air, at **a** no heat treatment, **b** 800 °C, **c** 900 °C, and **d** 1000 °C. The y-axis represents the square root of the intensity to magnify the presence of minor reflections
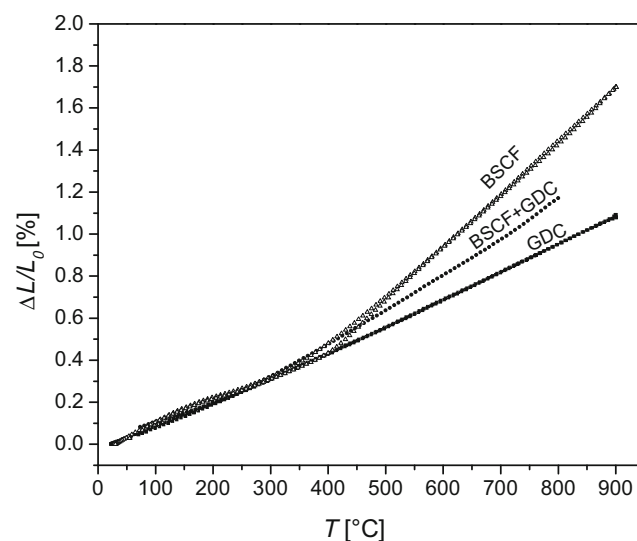

Fig. 4 $\Delta L/L_0$ vs. T curves for BSCF, the composite BSCF+GDC, and pure GDC in the temperature range $30 \leq T \leq 900$ °C, in air

Table 1 Linear expansion coefficient $\alpha = \Delta L/(L_0 \times \Delta T)$ (K^{-1}) for BSCF, the composite BSCF+GDC, and GDC. The values of α were calculated for the temperature ranges 80–300, 400–900, and 80–900 °C

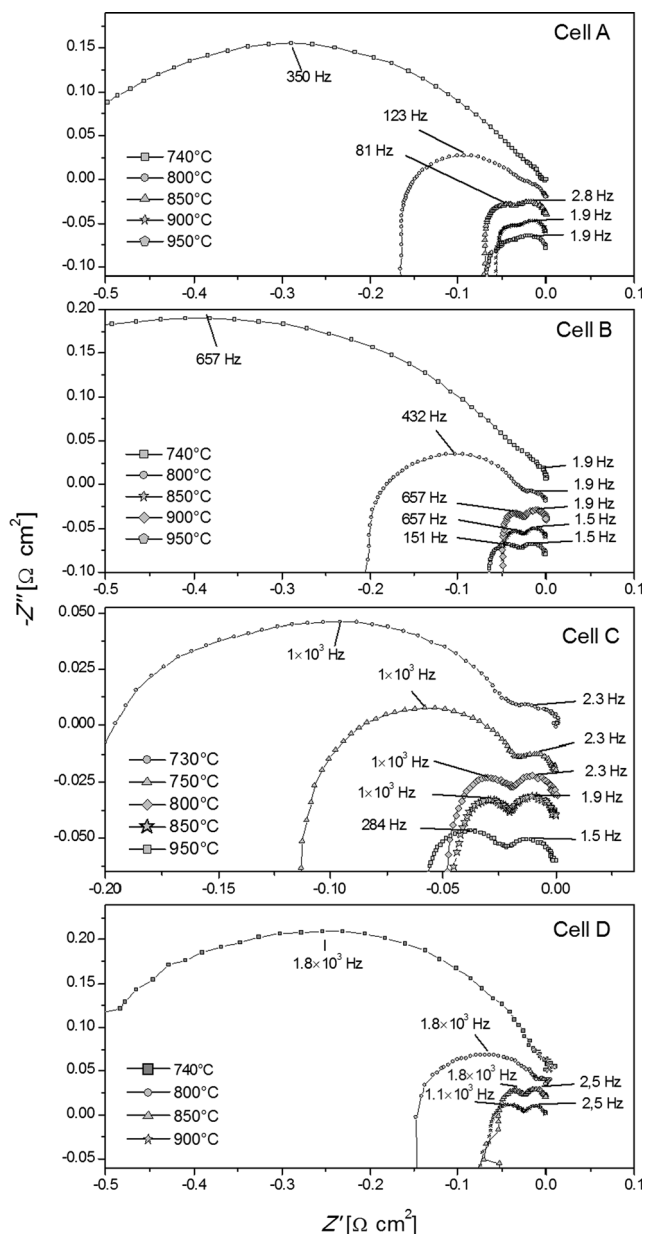| Compound	$\alpha_{80–300} \times 10^6$ (K^{-1})	$\alpha_{400–900} \times 10^6$ (K^{-1})	$\alpha_{80–900} \times 10^6$ (K^{-1})
BSCF	11.6 (1)	23.0 (1)	18.6 (2)
BSCF+GDC (1:1)	10.6 (2)	17.4 (2)	15.0 (1)
GDC	–	–	12.0 (1)

Fig. 5 Impedance spectra at $T = 600$ °C in air after the assemblage of layers forming the electrodes were heat treated at various temperatures between 750 and 950 °C. The $-Z''$ values were conveniently shifted to clearly show the experimental data

electrodes configuration. The Rp value for cell A (0.05 Ω cm^2) is slightly larger than the values obtained for cell C prepared with a graded electrode (0.039 Ω cm^2). Although the difference is very small, this tendency was also reported for La$_{0.4}$Ba$_{0.6}$CoO$_{3-\delta}$ [21]. Since the lower Rp values were obtained after the heat treatments at around 850–900 °C, the formation of a small fraction of BaCeO$_3$ at the interface BSCF/GDC is expected due to chemical reactivity. Yung et al. [30] have concluded that the formation of BaCeO$_3$ at the electrode/electrolyte interface is caused by the segregation of Ba from the crystal structure of BSCF due to the influence of temperature or cathode polarization, which tend to increase the electrode polarization resistance. On the other hand, Wang et al. [16] reported the formation of a negligible amount of the perovskite (Ba,Sr,Sm,Ce)(Co,Fe)O$_3$ and BaCeO$_3$ at the interface of BSCF/Ce$_{0.9}$Sm$_{0.1}$O$_{1.95}$ (SDC) when the electrode is heat treated at $900 \leq T \leq 1000$ °C, and the authors suggested it may contribute to reducing the interfacial resistance [16]. Our results show that the IF arc tends to increase when the heat treatment is carried out at temperatures above the optimum value, which suggests either that the formation of BaCeO$_3$ is not beneficial for the electrochemical response of the electrode or that the growth of the ceramic grains of BSCF decreases the active surface for the oxygen reduction reaction as suggested by Wang et al. [16].

Microstructure

The particle morphology of the layers forming the electrodes was observed by SEM microscopy. All the interfaces show good adhesion and connectivity. No delamination was observed, and the thicknesses of the layers were uniform. Figure 6 shows SEM micrographs of the electrodes cross-section of cells A–D after impedance spectroscopy measurements. In this figure, the thicknesses of the electrodes are approximately 30 μm and the sizes of the BSCF particles are in the range 1–5 μm, which is larger than the submicronic particles of the BSCF-750 material used to prepare the electrodes. The growth of ceramic grains takes place during the heat treatment at 850–900 °C where the electrodes are formed and the different layers attach to each other. Although this process reduces the electrode specific area of the BSCF material, it helps to obtain the minimum Rp value for the oxygen reduction reaction. On the other hand, the particle size of GDC used in the porous and composite layers remains in the range 0.1–0.5 μm with the variation of the heat treatment temperature.

Electrochemical measurements

The impedance spectroscopy measurements as a function of T and pO$_2$ were performed on cells heat treated at 900 °C for which the minimum Rp values were found ("Optimization of the heat treatment temperature for the cathode preparation"

Fig. 6 SEM micrographs (×1850) of the electrodes cross-section for configurations A, B, C, and D prepared with BSCF
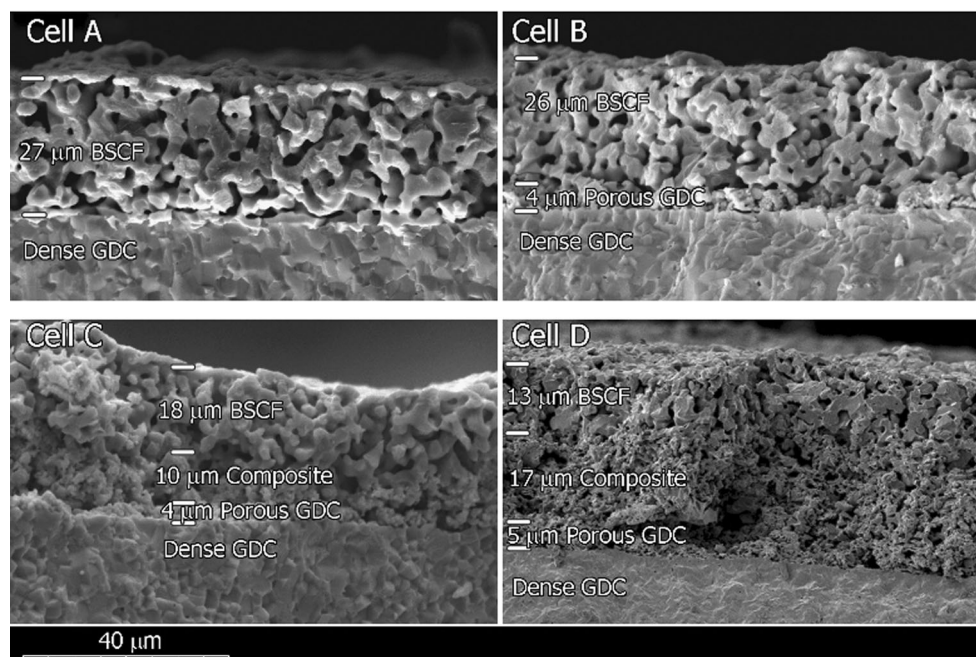
section) and the majority phase corresponds to the cubic perovskite BSCF ("Phase formation, chemical compatibility and expansion coefficient determination" section).

Variation of the impedance spectra with temperature

The variation of the impedance spectra with temperature in air shows overall similar behavior for the four cells, although some differences were observed at low temperatures. As an example, Fig. 7 displays the impedance spectra for cell C in the temperature range $400 \leq T \leq 800$ °C. At $T \geq 550$ °C, the impedance data consist of two arcs previously denominated IF and LF (see ("Optimization of the heat treatment temperature for the cathode preparation" section), with the LF contribution remaining almost constant with temperature. At $T \leq 550$ °C, the LF contribution becomes negligible compared to the IF arc; however, a third contribution denominated LF* and thermally activated was introduced to explain the low-frequency data at low temperature. A similar behavior was observed for cells A and B, while for cell D the LF* contribution was not detected. At low temperatures, we also observed a small arc at high frequency ($\nu > 10^4$) probably associated to a process taking place at the electrolyte, which we neglected in our analysis. Therefore, the equivalent circuit used to fit the impedance data consists of a pure resistance (R_E) in series with an inductance (L) in parallel with a resistance (R_{IN}) to simulate the electrolyte and the inductive contribution from the device and leads (see Fig. 8). Additionally, we added two elements (R_i, CPE_i) in series representing processes taking place at the electrode depending of the cell configuration and the temperature range. Figure 9 shows the Arrhenius plot for R_{LF}, R_{IF},

and R_{LF*}. The total polarization resistance Rp, also included in Fig. 9, was obtained from the addition of R_{LF}, R_{IF}, and R_{LF*}. At high temperatures, $T \geq 700$ °C, the LF response is the largest contribution for the four cells and at lower temperatures, $550 \leq T \leq 700$ °C, it is of the same order as the IF contribution; however, both arcs remain clearly distinguishable. R_{LF} has the particularity that it slightly increases with temperature and its value for $T \geq 550$ °C is in the range 0.025–0.035 Ω cm^2. Also, the apex frequency and the capacitance exhibit little variations between 1.5 and 3 Hz and 2.6 and 4.6 F/cm^2, respectively. These values were shown to be independent of the electrode design and also of the heat treatment temperature used for the cell preparation (see Fig. 5). Therefore, these data suggest that both the microstructure and the potential secondary phases present as a result of the final heat treatment barely affecting the R_{LF} contribution. In the temperature range $500 \leq T \leq 700$ °C, the IF response becomes visible, indicating a thermally activated process. The calculated activation energy values for R_{IF} were 0.59 (5), 0.77 (5), 1.08 (4), and 1.2 (1) eV for the electrodes A, B, C, and D, respectively. Our data show that R_{IF} depends on the heat treatment temperature ("Optimization of the heat treatment temperature for the cathode preparation" section) and also on the electrode configuration, in view that at $T \leq 550$ °C, the lowest R_{IF} values were obtained for cells A and B. The apex frequency of the IF contribution for all the cells varies approximately from 10 Hz at low temperatures up to 5×10^3 Hz at high temperatures, almost three orders of magnitude. On the other hand, the capacitance C_{IF} increases when the cell configuration varies from cell D to A. The highest capacitance values $C_{IF} \sim 1 \times 10^{-1}$ F/cm^2 were found for cell A, while the lowest
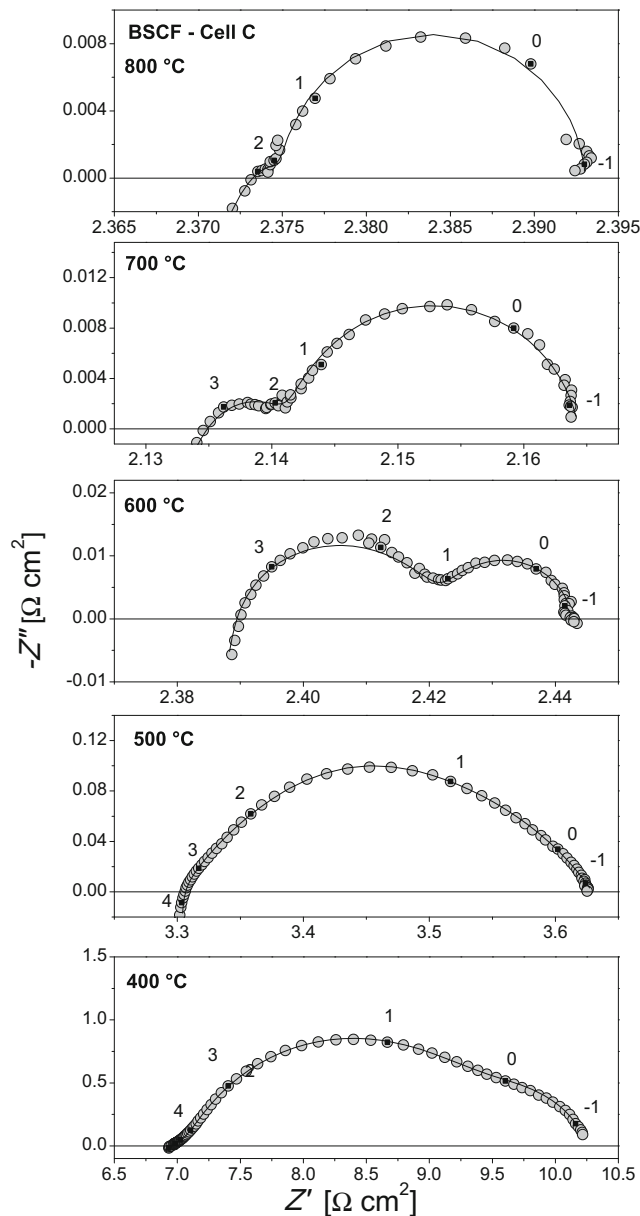
Fig. 7 Variation of the impedance spectra in the temperature range 400–900 °C in air for a BSCF electrode with the configuration of the cell C. The *solid line* corresponds to the fit of the experimental data. The logarithm of the frequency is indicated in the figure

values $C_{IF} \sim 5 \times 10^{-3}$ F/cm² correspond to cell D. The lower R_{IF} values obtained for cells A and B correlates with the presence of the LF* contribution which rises from cell C to A. LF* is thermally activated and its characteristic frequency reaches values as low as 0.01 Hz at 400 °C. For the R_{LF*} contribution,
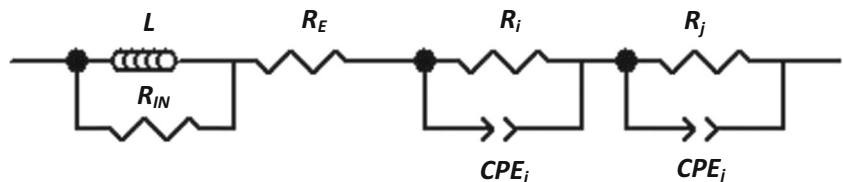
the obtained activation energy values were 1.39 (1) and 1.47 (2) eV for cells A and B, respectively. Figure 9a–d shows that at high temperatures $Rp \sim R_{LF}$, while at low temperatures $Rp \sim R_{LF*}$ for cells A and B and $Rp \sim R_{IF}$ for cells C and D. Previous results on cells type B prepared with $La_{0.3}Ba_{0.7}Co_{0.6}Fe_{0.4}O_{3-\delta}$ [14] show Rp is approximately four to ten times larger than the values obtained for BSCF, while for a cell C prepared with $La_{0.3}Ba_{0.7}CoO_{3-\delta}$ [15], the Rp values are of the same order. However, the impedance data was described in both cases with the same processes used in this work for BSCF.

Variation of the impedance spectra with the oxygen partial pressure

Aiming to understand the origin of the arcs forming the impedance spectra, we have carried out measurements keeping T constant and varying pO_2 in the range $1 \times 10^{-3} < pO_2 < 1$ atm. As an example, Fig. 10 shows the Nyquist diagram for the cell D at $T = 600$ °C. According to the previous section, only the IF and LF responses are expected at this temperature. The impedance diagram under pure oxygen ($pO_2 = 1$ atm) consists of only one arc with an apex frequency of ~750 Hz that corresponds to the IF response. As soon as the pO_2 decreases, a second contribution becomes visible at the low-frequency side, the LF response. Both contributions tend to increase as the pO_2 decreases, although the LF arc grows visibly faster. The lack of the LF response for $pO_2 = 1$ atm is consistent with the absence of the O_2 phase diffusion contribution due to the lack of an oxygen concentration gradient in the porous of the electrode [33, 34]. As the oxygen concentration decreases, this contribution becomes visible and its polarization resistance increases as is displayed in Fig. 10. The analysis of the polarization resistance data as a function of the pO_2 is usually made using the power law:

$$R \propto pO_2{}^n \tag{1}$$

where n is an exponent related with the species involved in the cathode reaction and the process responsible of the electrode polarization [35, 36]. Figure 11 shows the log $(R/\Omega$ cm²) vs. log (pO_2/atm) data for the polarization resistances Rp, R_{LF}, and R_{IF} at $T = 600$ °C for cells A, B, C, and D, obtained using the equivalent circuit shown in Fig. 8. Noteworthy, the linear fit of the log $(R_{LF}/\Omega$ cm²) vs. log (pO_2/atm) data gives slope

Fig. 8 Equivalent circuit used to fit the impedance spectra. For cells C and D, $R_i = R_{IF}$ and $R_j = R_{LF}$. For cells A and B at $T > 550$ °C $R_i = R_{IF}$ and R_{LF} while at $T \leq 550$ °C $R_i = R_{IF}$ and R_{LF*}

Fig. 9 Arrhenius plot of the total polarization resistance R_p for cells A, B, C, and D using BSCF as electrode material and also of the polarization resistances R_{IF}, R_{LF}, and R_{LF*} obtained from the fit of the impedance spectra

Fig. 10 Variation of the impedance spectra as a function of pO_2 at 600 °C for cell A
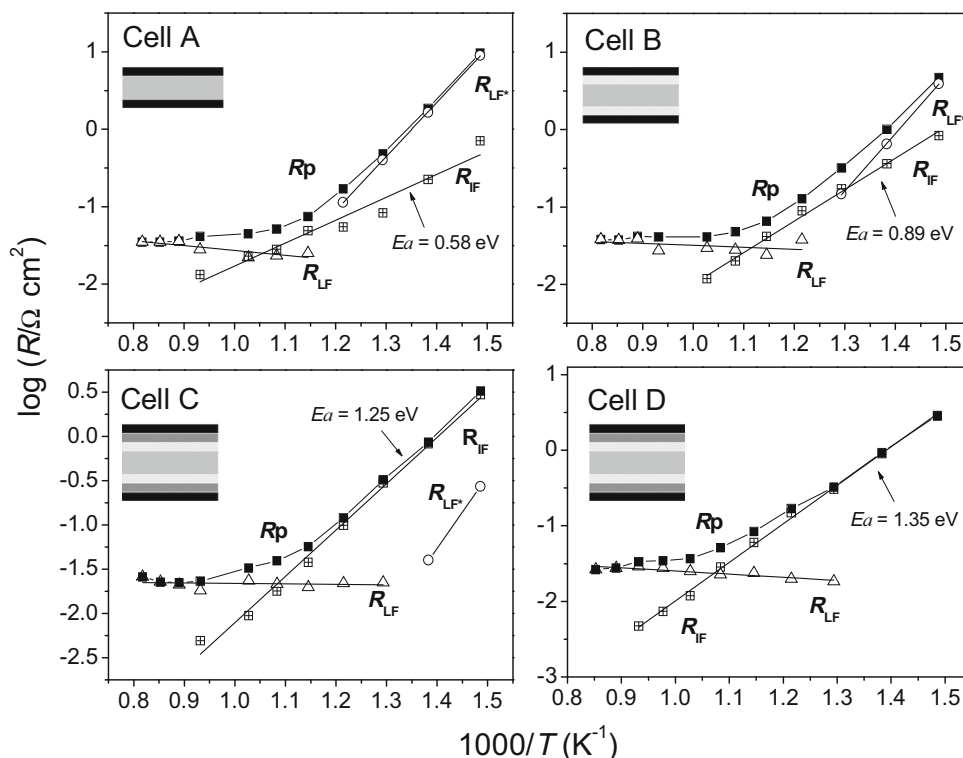
values close to $n \sim -1$ for all the electrode configurations, this is in agreement with the existence of a process controlled by the oxygen gas phase diffusion [14, 33, 37–39]. Additionally, the capacitance values obtained for this contribution, which are between 1.5 and 4 F/cm², and their weak dependence on

temperature are expected characteristics for this process [23, 39, 40]. Using Eq. 1, we also calculated from the data displayed in Fig. 11 the parameter n for the R_{IF} contribution. The obtained values were $n = -0.07(2)$, $-0.10(2)$, $-0.30(2)$, and $-0.43(3)$ for cells A, B, C, and D, respectively. A value of $n \approx -0.25$ is usually assigned to charge-transfer process including reduction of the adsorbed atomic oxygen followed by the oxide ion incorporation into the electrode, $n \approx -0.5$ to the dissociation of molecular oxygen to atomic oxygen at the surface of the electrode, and $n \approx -1$ to the adsorption of molecular oxygen to the electrode surface [35, 41, 42]. A weak dependence on pO_2 at high frequencies was ascribed to the oxide ion transfer across the cathode/electrolyte interface [41, 43]. Our data show that the parameter n of the R_{IF} contribution tends to become more negative as the number of layers forming the electrode increases, which correlates with the increment of the electrode surface area and the BSCF/GDC interface. Thus, while the contact areas between electrode and electrolyte for cell A are constrained to the surface defined by the dense electrolyte, it is reasonable to assume that for cell B, the introduction of an irregular porous layer of GDC between the electrode and the dense electrolyte slightly increases the BSCF/GDC interface area giving place to a minor variation on n. This progression was strengthened in cells C and D with the fabrication of graded cathodes through the introduction of a BSCF+GDC composite layer using GDC with increasing surface area. For these cells, the parameter n reaches the values $-0.30(2)$ and $-0.43(3)$. Thus, the inclusion of the
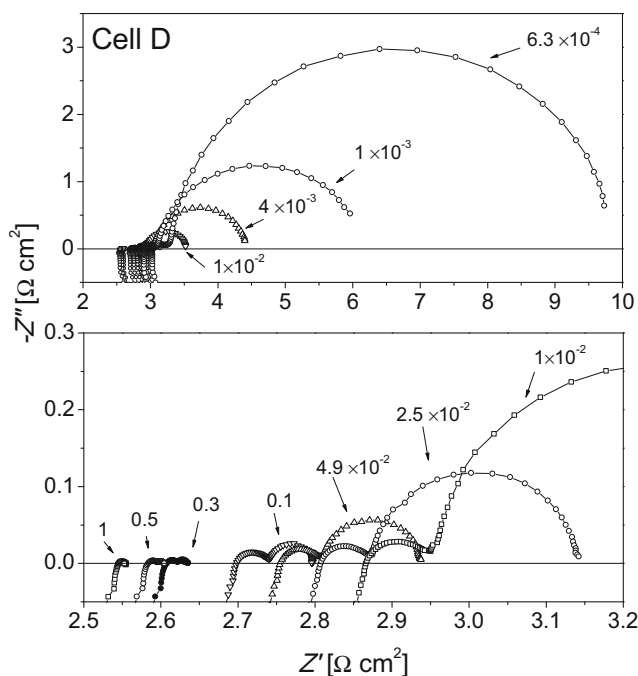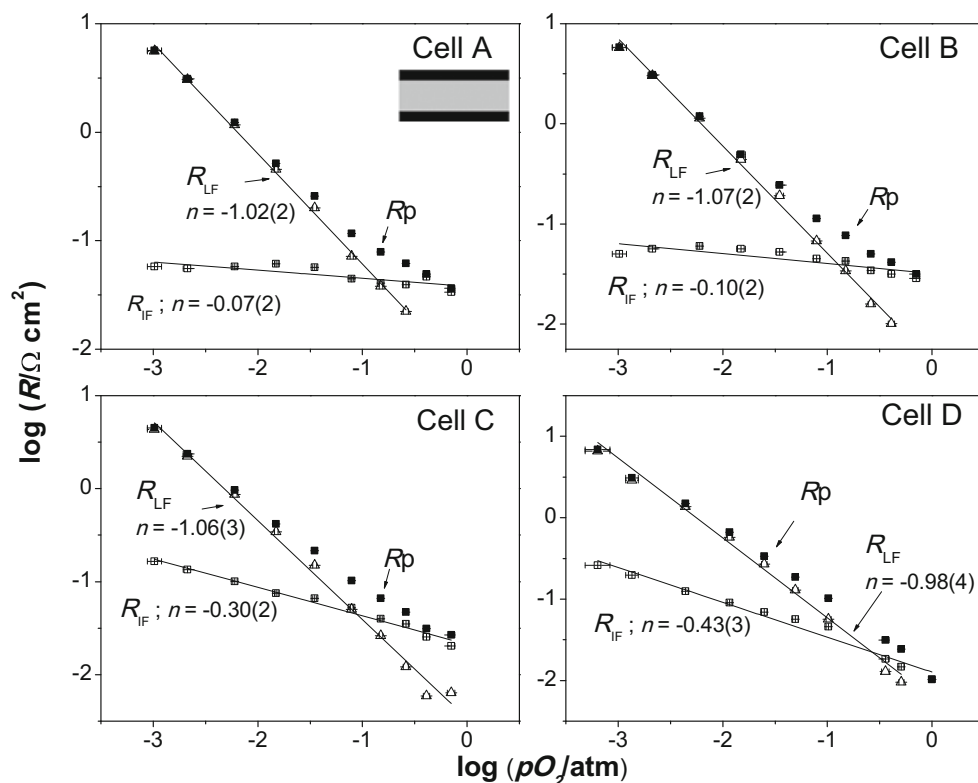
Fig. 11 Variation of the total polarization resistance R_p and the polarization resistances R_{IF} and R_{LF} with the oxygen partial pressure at 600 °C for cells A, B, C, and D with electrodes prepared with BSCF

composite layer is responsible for the change of the rate-limiting mechanism from a mixed kinetics between the oxide ion transfer across the electrode/electrolyte interface and charge transfer at the electrode surface ($n \sim -0.1$), to a mixed kinetics between charge transfer and molecular oxygen dissociation at the electrode surface ($n \sim -0.4$). The larger BSCF/GDC interface area seems to be responsible that the oxide ion transfer is not the limiting step of the IF process for cells C and D, regardless of the chemical reactivity at the interface during the heat treatment at ~900 °C.

Variation of the impedance spectra with T and pO$_2$ for cells A and D

At $T = 600$ °C, the LF* contribution results negligible for cells A and B. Thus, we have measured the impedance spectra at $T = 450$ °C in a cell type A to study the behavior of the LF* and IF contributions as a function of pO$_2$. The variations of R_{IF}, R_{LF*}, and R_p are shown in Fig. 12. The values of the parameter n were $n = -0.54(3)$ and $-0.11(1)$ for the LF* and the IF responses, respectively. The capacitance values of the LF* contribution were stable at $C_{LF*} \sim 1.3-1.5$ F/cm^2. These values are very large; however, as the LF* contribution was found thermally activated we ruled out the molecular oxygen diffusion at the gas phase. In addition, the low characteristic frequency values of the LF* arc, which vary from 7×10^{-3} to

0.24 Hz as the pO$_2$ increases from 1×10^{-3} to 0.45 atm, makes the assignment of the LF* contribution uncertain.

We have also studied the electrochemical response as a function of pO$_2$ at various temperatures of cell D, which shows the lower R_p value [21]. Figure 13 shows the variation of R_p, R_{IF}, and R_{LF} with pO$_2$ at 450, 600, and 850 °C and the parameter n value for the LF and IF responses. One more time,
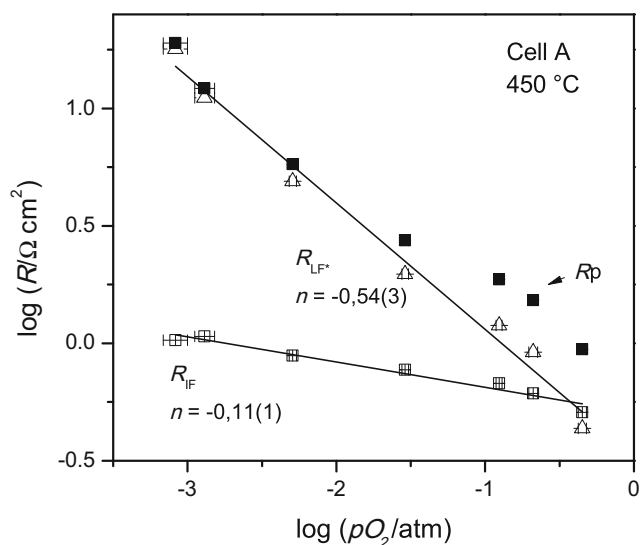

Fig. 12 Variation of R_p, R_{LF*}, and R_{IF} as a function of pO$_2$ for electrode A at 450 °C
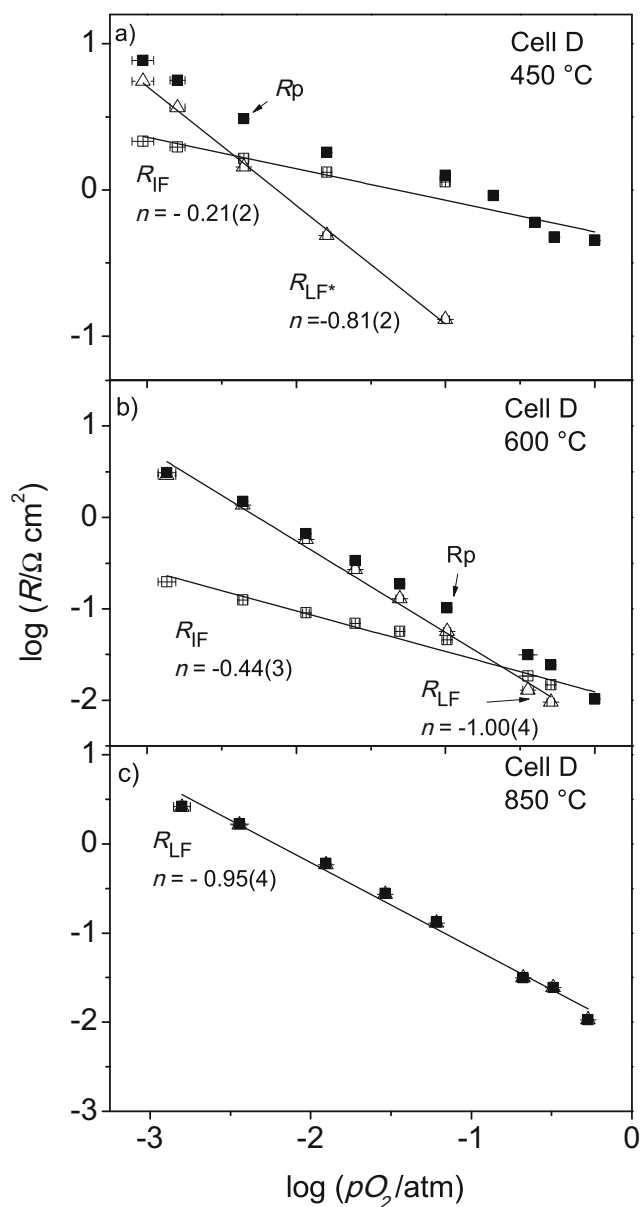
Fig. 13 Variation of Rp, R_{LF*}, and R_{IF} as a function of pO2 for electrode D at **a** 450 °C, **b** 600 °C, and **c** 850 °C

independently of the temperature, we have obtained $n \sim -1$ for R_{LF}, which confirm that this arc corresponds to the gas phase diffusion contribution. On the other hand, the parameter n for the IF response tend to be more negative with the increase of temperature. The computed values were $n = -0.21(2)$, $-0.44(3)$ for 450 and 600 °C, respectively. These data indicate that the rate-limiting step varies with temperature from charge transfer at the electrode surface at 450 °C to molecular oxygen dissociation at 600 °C. At 850 °C, the impedance data for the IF arc are negligible compared to the LF response; therefore, the errors in the parameter n value may hamper a correct assignment. This behavior is in agreement with previous works, where the absolute value of n tends to increase with temperature [17, 38, 41].

Conclusions

The precursor of the BSCF material was prepared by an acetic acid-based gel route and heat treated at 750 °C. At this temperature, a cubic perovskite coexists with a 2H hexagonal phase. The pure cubic perovskite $Ba_{0.5}Sr_{0.5}Co_{0.8}Fe_{0.2}O_{3-\delta}$ was obtained at 1000 °C. The chemical reactivity with GDC was detected by XRD at $T \geq 900$ °C due to the appearance of small reflections of $BaCeO_3$. Four electrode configurations, from a single layer to a graded cathode of BSCF, were used to study the electrochemical response by impedance spectroscopy. The optimum heat treatment temperature for the electrodes was monitored by impedance spectroscopy. The minimum polarization resistances were obtained after the heat treatment at 850–900 °C during 1 h in air. The total polarization resistance values at 600 °C were as low as $Rp = 0.04$–0.05 Ω cm² for the four cells. These data show that low values of Rp can be obtained when the electrode configuration and the heat treatment temperature for the electrode assembly are optimized. The impedance spectra consist of a low-frequency (LF) and an intermediate-frequency (IF) complex impedance arc. A third process was identified at low frequency (LF*) for cells A and B at low temperatures. The polarization resistance R_{LF} predominates at high temperature and it corresponds to molecular oxygen gas phase diffusion. This contribution shows no variation with the cell configuration. At lower temperatures, the IF response is the rate-limiting step for cells C and D with a composite layer. Impedance spectra as a function of the pO2 show that the parameter n changes from ~ -0.1 (cells A and B) to -0.4 (cells C and D). This result indicates the IF contribution shifts from a mixed kinetics between the oxide ion transfer across the electrode/electrolyte interface and charge transfer at the electrode surface ($n \sim -0.1$) for cells A and B, to a mixed kinetics between charge transfer and molecular oxygen dissociation at the electrode surface ($n \sim -0.4$) for cells C and D. This behavior could be related to the increase of the electrode/electrolyte area when the cell changes from type A to D.

References

1. Jacobson A (2010) Materials for solid oxide fuel cells. Chem Mater 22:660–674
2. Kilner J, Burriel M (2014) Materials for intermediate-temperature solid-oxide fuel cells. Annu Rev Mater Res 44:365–393

3. Shao Z, Dong H, Xiong G, Cong Y, Yang W (2001) Performance of a mixed-conducting ceramic membrane reactor with high oxygen permeability for methane conversion. J Membr Sci 183:181–192

4. Zhou W, Ran R, Shao Z (2009) Progress in understanding and development of $Ba_{0.5}Sr_{0.5}Co_{0.8}Fe_2O_{3-\delta}$ - based cathodes for intermediate-temperature solid-oxide fuel cells: a review. J Power Sources 192:231–246

5. Liu LM, Lee TH, Qiu L, Yang YL, Jacobson A (1996) A thermogravimetric study of the phase diagram of strontium cobalt iron oxide, $SrCo_{0.8}Fe_{0.2}O_{3-\delta}$. Mater Res Bull 31:29–35

6. Grunbaum N, Mogni L, Prado F, Caneiro A (2004) Phase equilibrium and electrical conductivity of $SrCo_{0.8}Fe_{0.2}O_{3-\delta}$. J Solid State Chem 177:2350–2357

7. Prado F, Grunbaum N, Caneiro A, Manthiram A (2004) Effect of La^{3+} doping on the perovskite-to-brownmillerite transformation in $Sr_{1-x}La_xCo_{0.8}Fe_{0.2}O_{3-\delta}$ ($0 \le x \le 0.4$). Solid State Ionics 167:147–154

8. Shao Z, Haile SM (2004) A high-performance cathode for the next generation of solid-oxide fuel cells. Nature 431:170–173

9. Švarcová S, Wiik K, Tolchard J, Bouwmeester HJM, Grande T (2008) Structural instability of cubic perovskite $Ba_xSr_{1-x}Co_{1-y}Fe_yO_{3-\delta}$. Solid State Ionics 178:1787–1791

10. Arnold M, Gesing T, Martynczuk J, Feldhoff A (2008) Correlation of the formation and the decomposition process of the BSCF perovskite at intermediate temperatures. Chem Mater 20:5851–5858

11. Petric A, Huang P, Tietz F (2000) Evaluation of La–Sr–Co–Fe–O perovskites for solid oxide fuel cells and gas separation membranes. Solid State Ionics 135:719–725

12. Zhu Q, Jin T, Wang Y (2006) Thermal expansion behavior and chemical compatibility of $Ba_xSr_{1-x}Co_{1-y}Fe_yO_{3-\delta}$ with 8YSZ and 20GDC. Solid State Ionics 177:1199–1204

13. Xie J, Ju Y, Sakai T, Ishihara T (2013) Improvement in stability of $La_{0.4}Ba_{0.6}CoO_3$ cathode by combination with $La_{0.6}Sr_{0.4}Co_{0.2}Fe_{0.8}O_3$ for intermediate temperature-solid oxide fuel cell. J Solid State Electrochem 17:2251–2258

14. Setevich C, Prado F, Florio DZ, Caneiro A (2014) Stabilization of the cubic perovskite in the system $La_{1-x}Ba_xCo_{1-y}Fe_yO_{3-\delta}$ ($0.7 \le x \le 0.9$) and its electrochemical performance as cathode materials for IT-SOFC. J Power Sources 247:264–272

15. Setevich C, Mogni L, Caneiro A, Prado F (2012) Characterization of the $La_{1-x}Ba_xCoO_{3-\delta}$ ($0 \le x \le 1$) system as cathode material for IT-SOFC. J Electrochem Soc 159:B72–B79

16. Wang K, Ran R, Zhou W, Gu H, Shao Z, Ahn J (2008) Properties and performance of $Ba_{0.5}Sr_{0.5}Co_{0.8}Fe_2O_{3-\delta}$ + $Sm_{0.2}Ce_{0.8}O_{1.9}$ composite cathode. J Power Sources 179:60–68

17. Liu QL, Khor KA, Chan SH (2006) High-performance low-temperature solid oxide fuel cell with novel BSCF cathode. J Power Sources 161:123–128

18. Lee JG, Ho Park J, Gun Shul Y (2014) Tailoring gadolinium-doped ceria-based solid oxide fuel cells to achieve 2 W cm^{-2} at 550 °C. Nat Commun 5:4045

19. Yaremchenko A, Mikhalev S, Kravchenko E, Frade J (2014) Thermochemical expansion of mixedconducting (Ba, Sr) $Co_{0.8}Fe_{0.2}O_{3-\delta}$ ceramics. J Eur Ceram Soc 34:703–715

20. Li R, Ge L, Chen H, Guo L (2012) Preparation and performance of triple-layer graded $LaBaCo_2O_{5+\delta}$–$Ce_{0.8}Sm_{0.2}O_{1.9}$ composite cathode for intermediate-temperature solid oxide fuel cells. Electrochim Acta 85:273–277

21. Setevich C, Mogni L, Caneiro A, Prado F (2012) Optimum cathode configuration for IT-SOFC using $La_{0.4}Ba_{0.6}CoO_{3-\delta}$ and $Ce_{0.9}Gd_{0.1}O_{1.95}$. Int J Hydrogen Energy 37:14895–14901

22. Murray EP, Server MJ, Barnett SA (2002) Electrochemical performance of (La, Sr)(Co, Fe)O_3–(Ce, Gd)O_3 composite cathodes. Solid State Ionics 148:27–34

23. Gu H, Chen H, Gao L, Guo L (2009) Electrochemical properties of $LaBaCo_2O_{5+\delta}$–$Sm_{0.2}Ce_{0.8}O_{1.9}$ composite cathodes for intermediate-temperature solid oxide fuel cells. Electrochim Acta 54:7094–7098

24. Chen D, Ran R, Shao Z (2010) Assessment of $PrBaCo_2O_{5+\delta}$+ $Sm_{0.2}Ce_{0.8}O_{1.9}$ composites prepared by physical mixing as electrodes of solid oxide fuel cells. J Power Sources 195:7187–7195

25. Xia C, Rauch W, Chen F, Liu M (2002) $Sm_{0.5}Sr_{0.5}CoO_3$ cathodes for low-temperature SOFCs. Solid State Ionics 149:11–19

26. Xia Y, Armstrong T, Prado F, Manthiram A (2000) Sol–gel synthesis, phase relationships, and oxygen permeation properties of $Sr_4Fe_{6-x}Co_xO_{13+\delta}$ ($0 \le x \le 3$). Solid State Ionics 130:81–90

27. Rodríguez-Carvajal J Fullprof: a program for Rietveld Refinement and Profile Matching Analysis of Complex Powder Diffraction Patterns. Laboratoire Léon Brillouin (CEA-CNRS)

28. Zview version 2.9b. Copyright 1990–2005. Scribner Associates, Inc. D. Johnson

29. Taguchi H, Takeda Y, Kanamaru F, Shimada M, Koizumi M (1977) Barium cobalt trioxide. Acta Crystallogr B 33:1298–1299

30. Yung H, Jian L, Ping Jiang S (2012) Polarization promoted chemical reaction between $Ba_{0.5}Sr_{0.5}Co_{0.8}Fe_{0.2}O_{3-\delta}$ cathode and ceria based electrolytes of solid oxide fuel cells. J Electrochem Soc 159:F794–F798

31. Zhou W, Ran R, Shao Z, Jin W, Xu N (2008) Evaluation of A-site cation-deficient $(Ba_{0.5}Sr_{0.5})_{1-x}Co_{0.8}Fe_{0.2}O_{3-\delta}$ ($x>0$) perovskite as a solid-oxide fuel cell cathode. J Power Sources 182:24–31

32. Adler SB (2001) Chemical expansivity of electrochemical ceramics. J Am Ceram Soc 84:2117–2119

33. Deportes C, Duclot M, Fabry P, Fouletier J, Hammou A, Kleitz M, Siebert E, Souquet JL (1994) Electrochimie des Solides. Presses Universitaires de Grenoble, Grenoble

34. Huang K (2004) Gas-diffusion process in a tubular cathode substrate of a SOFC. II: identification of gas-diffusion process using AC impedance method. J Electrochem Soc 151:H117–H121

35. Takeda Y, Kanno R, Noda M, Tomoda Y, Yamamoto O (1987) Cathodic polarization phenomena of perovskite oxide electrodes with stabilized zirconia. J Electrochem Soc 134:2656–2661

36. Ringuedé A, Fouletier J (2001) Oxygen reaction on strontium-doped lanthanum cobaltite dense electrodes at intermediate temperatures. Solid State Ionics 139:167–177

37. Grunbaum N, Dessemond L, Fouletier J, Prado F, Caneiro A (2009) Rate limiting steps of the porous $La_{0.6}Sr_{0.4}Co_{0.2}Fe_{0.2}O_{3-\delta}$ electrode material. Solid State Ionics 180:1448–1452

38. Mogni L, Grunbaum N, Prado F, Caneiro A (2011) Oxygen reduction reaction on Ruddlesden–Popper phases studied by impedance spectroscopy. J Electrochem Soc 158:B202–B207

39. Adler SB (2004) Factors governing oxygen reduction in solid oxide fuel cell cathodes. Chem Rev 104:4791–4843

40. Reid RC, Prausnitz JM, Poling BE (2001) The properties of Gases and Liquids, 5th edn. Mc Graw-Hill, New York

41. Pang S, Jiang X, Li X, Wang Q, Su Z (2012) A comparative study of electrochemical performance of $La_{0.5}Ba_{0.5}CoO_{3-\delta}$ and $La_{0.5}Ba_{0.5}CoO_{3-\delta}$-$Gd_{0.1}Ce_{0.9}O_{1.95}$ cathodes. Int J Hydrogen Energy 37:2157–2165

42. Chen D, Ran R, Zhang K, Wang J, Shao Z (2009) Intermediate-temperature electrochemical performance of a polycrystalline $PrBaCo_2O_{5+\delta}$ cathode on samarium-doped ceria electrolyte. J Power Sources 188:96–105

43. Escudero MJ, Aguadero A, Alonso JA, Daza L (2007) A kinetic study of oxygen reduction reaction on La NiO cathodes by means of impedance spectroscopy. J Electroanal Chem 611:107–116